Quantum multifractality as a probe of phase space in the Dicke model

M. A. Bastarrachea-Magnani [1], D. Villaseñor [2], J. Chávez-Carlos [3], S. Lerma-Hernández [4],
L. F. Santos [3], and J. G. Hirsch [5]

[1]*Departamento de Física, Universidad Autónoma Metropolitana-Iztapalapa, Av. Ferrocarril San Rafael Atlixco 186,
C.P. 09310 Mexico City, Mexico*

[2]*Instituto de Investigaciones en Matemáticas Aplicadas y en Sistemas, Universidad Nacional Autónoma de México,
C.P. 04510, Mexico City, Mexico*

[3]*Department of Physics, University of Connecticut, Storrs, Connecticut 06269, USA*

[4]*Facultad de Física, Universidad Veracruzana, Campus Arco Sur, Paseo 112, C.P. 91097 Xalapa, Mexico*

[5]*Instituto de Ciencias Nucleares, Universidad Nacional Autónoma de México, Apdo. Postal 70-543, C.P. 04510 Mexico City, Mexico*

We study the multifractal behavior of coherent states projected in the energy eigenbasis of the spin-boson Dicke Hamiltonian, a paradigmatic model describing the collective interaction between a single bosonic mode and a set of two-level systems. By examining the linear approximation and parabolic correction to the mass exponents, we find ergodic and multifractal coherent states and show that they reflect details of the structure of the classical phase space, including chaos, regularity, and features of localization. The analysis of multifractality stands as a sensitive tool to detect changes and structures in phase space, complementary to classical tools to investigate it. We also address the difficulties involved in the multifractal analyses of systems with unbounded Hilbert spaces.

I. INTRODUCTION

Mandelbrot first introduced the notion of multifractality to describe the statistical properties of turbulent flows [1]. Multifractality is characterized by an infinite set of critical exponents that determine the scaling of the moments of the distribution of some quantity. It has been observed in a wide range of phenomena, from mathematical objects, such as strange attractors [2–4] and diffusion-limited aggregates [5], to the human heartbeat series [6] and brain activity [7]. In the last two decades, the subject has gained attention in the quantum domain, for both disordered and clean systems, in relation to problems, such as the Anderson localization phenomena [8–11], many-body localization [12–15], quantum phase transitions [16], disordered Josephson junctions [17], the Bose-Josephson junction [18], Floquet eigenstates [19–21], quantum phases in spin chains [22], quantum maps [23], robustness against perturbations [24,25], open quantum systems [26], quantum scarring [27], and applications to quantum computing [28].

In quantum mechanics, multifractality roughly means that the wave function is extended but effectively restricted to a portion of the Hilbert space [29,30]. This restriction happens because the weight of each component of the wave function scales differently and independently when the Hilbert space dimension increases. Each weight is a fractal on its own, hence the name multifractal. Quantum multifractality is intertwined with the concepts of localization, ergodicity, and chaos [31] and was recently used as a local measure of chaos for the kicked top model [32]. In this work, we perform quantum multifractal analyses to examine and compare the classically chaotic and regular structures of the phase space of the Dicke model, in the same spirit as what was done in Ref. [33],

where a measure of quantum state localization, the so-called participation ratio, was used to probe classical chaos in that model.

The spin-boson Dicke model describes a bosonic field strongly interacting with the collective degrees of freedom of $\mathcal{N}$ two-level systems (qubits) [34]. It has drawn attention in recent years not only because it is the most simple, yet nontrivial, interacting model for exploring equilibrium and nonequilibrium properties [35–38], but also because it can be realized in various experimental setups, such as neutral atoms [39–42], ion traps [43,44], and Raman cavities [45,46]. One of the most prominent features of the model is the prediction of the transition to a superradiant quantum phase. In addition, the system's spectrum exhibits a transition from regularity to chaos as the energy increases [47–49], thus granting a fertile ground for exploring the onset of (multi)fractality.

Multifractality was recently studied in an interacting Tavis-Cummings model [50] (an integrable version of the Dicke model without the counter-rotating terms), where the eigenstates written in the computational basis were shown to be nonergodic. Fractality was also identified in the ground state of both the standard and anisotropic Dicke models [51,52]. However, investigating multifractality for energies above the ground state is challenging, because the model has an unbounded Hilbert space, and the study of multifractality relies on scaling analysis.

Here, we explore the multifractal behavior of coherent states spanned by the eigenbasis of the Dicke Hamiltonian. Each coherent state represents a point in the phase space where it is centered. We show that the analysis of quantum multifractality can be used as a probe to identify chaos and regularity.

The paper is organized as follows. In Sec. II, we describe the formalism for classical and quantum multifractality. In Sec. III, we present the Dicke Hamiltonian, its classical limit, and the general protocol to study the multifractality of coherent states. In Sec. IV, we analyze the fractal dimension of representative coherent states, and in Sec. V, we explore the overall behavior of multifractality over phase space structures across different energy surfaces. Finally, in Sec. VI, we offer our perspectives and conclusions. We also include appendices with further technical details.

II. FRACTAL ANALYSIS

Generally speaking, multifractality is a tool for characterizing, in a statistical sense, the nature of a local positive measure, that is, how a positive quantity is distributed on a set supporting that measure [53,54]. The scaling of the measure provides information about the measure's singular local behavior.

A. Multifractality quantification

In mathematics, to describe the dimensionality of an object quantitatively, one divides it into N pieces labeled by $k = 1, \ldots, N$, and considers an event occurring upon the object at the piece k with a probability p_k, which is given by the measure $d\mu$ or resolution length [53]. Next, one defines the partition function,

$$Z(q) = \sum_{k=1}^{N} p_k^q, \tag{1}$$

where $Z(1) = 1$ to fulfill normalization. The partition function provides global, quantitative information on the local behavior of the measure around each piece. As $N \to \infty$, the size of each piece decreases as N^{-1}, and the scaling behavior of the partition function is given by $Z(q) \sim N^{-\tau_q}$, where τ_q denotes the scaling in terms of q only, and $\tau_{q=1} = 0$ due to normalization. The exponents τ_q are called mass or homogeneity exponents [55].

The measure is multifractal when τ_q is a nonlinear function of q. This is expressed by parametrizing the mass exponents as

$$\tau_q = D_q(q-1), \tag{2}$$

where D_q is the generalized (Rényi) dimension [56,57] defined as

$$D_q = \lim_{N \to \infty} \left(\frac{1}{1-q} \frac{\log Z(q)}{\log N} \right). \tag{3}$$

For $q = 0$, the partition function counts the number of nonempty pieces of size N^{-1}, so $\tau_0 = -D_0 = -D$, where D is called Hausdorff fractal dimension or capacity of the support of the measure [55]. When D_q is a constant function of q, the system is monofractal with dimension D. This also includes objects of integer dimension (typically considered nonfractals). The generalized dimensions have specific names for some values of q. D_1 is called information dimension, because it measures the information gained by observing a system's trajectory with some precision and quantifying the Kolmogorov-Sinai entropy after a long time

of observation [58]. D_2 is known as the correlation dimension of the measure [2,3], because it corresponds to the scaling of the correlation between two points in the classical phase space. It has been conjectured that in the case of strange attractors, D_1 and D_2 are related to the Lyapunov exponents [59].

The mass exponents and the generalized dimensions follow some rules that need to be observed [55]. The exponents τ_q must be monotonically increasing functions with negative curvature [57]. Hence, it holds that $d\tau_q/dq > 0$ and $d^2\tau_q/dq^2 \leqslant 0$. Instead, the generalized dimensions D_q are positive monotonically decreasing functions of q bounded by $D_{\pm\infty} = D(q \to \pm\infty)$ [60]. Thus, $dD_q/dq \leqslant 0$, and $0 \leqslant D_\infty \leqslant D_q \leqslant D_{-\infty}$.

B. Quantum multifractality

One way to bring the concept of multifractality to the quantum realm is in terms of the level of delocalization of a quantum state written in a given basis. Consider a quantum state $|\Psi\rangle$ and a complete basis $\{|k\rangle\}$ over a Hilbert space of dimension $\aleph$. The probability of finding the quantum state in one of the elements of the basis is given by $|c_k|^2 = |\langle k|\Psi\rangle|^2$, which plays the role of the probability of finding the state (the event) over a given eigenstate (the piece). Thus, in this case, the partition function can be built in terms of the generalized inverse participation ratios [61] as

$$Z(q) = \text{IPR}_q = \sum_{k=1}^{\aleph} |c_k|^{2q}, \tag{4}$$

Here, the defining integrated measure is the normalization condition, so $\text{IPR}_{q=1} = 1$. The case $q = 2$ corresponds to the standard inverse participation ratio (IPR) [62,63]. The scaling of IPR_q with the size of the Hilbert space reveals the asymptotic statistics of the participation of the basis elements $|k\rangle$ in the state $|\Psi\rangle$ and is expected to be of the form $\text{IPR}_q \sim \aleph^{-\tau_q}$, where the exponents τ_q are now defined as

$$\tau_q := -\lim_{\aleph \to \infty} \frac{\log \text{IPR}_q}{\log(\aleph)}. \tag{5}$$

The scaling of IPR_q for all q is used to classify the states. Localized states have $D_q = 0$, extended but nonergodic states have $0 \leqslant D_q < 1$, and ergodic states imply $D_q = 1$. Multifractal wave functions are nonergodic extended states, because the ratio between the effective portion of the Hilbert space that they occupy and the full size of the Hilbert space is neither one nor vanishing as the system size increases [16]. In condensed matter, systems classified as insulators have $D_q = 0$, and conductors have $D_q \neq 0$ [61]. However, a full theory linking specific nonlinear behaviors of either τ_q or D_q to specific physical phenomena for all values of q is, in general, absent. Depending on the system, the connection is usually made ad hoc.

To determine whether τ_q is nonlinear, one resorts to the so-called anomalous scaling exponent,

$$\Delta_q = \tau_q - D(q-1), \tag{6}$$

which quantifies the deviation of the mass exponents from the linear behavior [61]. In the above equation, D is the linear

approximation to D_q. If the behavior of the mass exponents with q is parabolic and the anomalous fractal dimension is quadratic, $\Delta_q \approx \Delta(1-q)q$, with Δ constant, then we have *weak multifractality*, a concept introduced as an effort to provide a first approximation for multifractal behavior. Some symmetries have been proved for the anomalous fractal dimension, such as the reciprocity relation $\Delta_q = \Delta_{1-q}$ [8,64,65], that has been predicted to be valid for transitions belonging to the Wigner-Dyson classes. Efforts have been made to show its universality, being proved in some cases including the critical point of the Anderson localization transition [8,66–68], the power-law banded random matrix [69], and the integral quantum Hall effect [70]. Conversely, it has been found that the relation is not fulfilled when mechanisms like Gaussian fluctuations at small scales or algebraic localization of the wave function are present, such as in Floquet critical systems and random graphs [71]. However, as is discussed below, given numerical convergence constraints, we cannot verify this relation systematically for the Dicke model.

In what follows, we investigate linear and quadratic fits for τ_q as a function of q and then use Eq. (6) to obtain the approximate values to D and Δ. If the linear fit of τ_q is very good, then $\Delta \simeq 0$, so the system is closer to a monofractal.

III. DICKE HAMILTONIAN

The spin-boson Dicke Hamiltonian is given by

$$\hat{H}_D = \omega \hat{a}^\dagger \hat{a} + \omega_0 \hat{J}_z + \frac{\Omega}{\sqrt{\mathcal{N}}}(\hat{a}^\dagger + \hat{a})\hat{J}_x, \qquad (7)$$

where $\hbar = 1$, $\hat{a}^\dagger$ ($\hat{a}$) is the bosonic creation (annihilation) operator, and $\hat{J}_{x,y,z} = \frac{1}{2}\sum_{i=1}^{\mathcal{N}} \hat{\sigma}_{x,y,z}^i$ are collective pseudospin operators satisfying the su(2) algebra, with each Pauli matrix $\hat{\sigma}_{x,y,z}^i$ describing a single spin-1/2 (qubit). Here, ω, ω_0, and Ω are the boson, single qubit, and Rabi energy splittings. The Hamiltonian has two symmetries. First, it commutes with the total pseudospin length operator $\hat{\mathbf{J}}^2 = \hat{J}_x^2 + \hat{J}_y^2 + \hat{J}_z^2$, so the Hilbert space is divided into different subspaces corresponding to the pseudospin length j. The ground state of the collective system lies on the totally symmetric subspace with maximum pseudospin length $j = \mathcal{N}/2$, where the collective degrees of freedom are equivalent to bosons. Second, the Hamiltonian commutes with a discrete parity operator, $\hat{\Pi} = \exp[i\pi(\hat{a}^\dagger \hat{a} + \hat{J}_z + j\hat{\mathbb{1}})]$, which leads to the further separation of the Hilbert space into two subspaces corresponding to each parity value.

An advantage of working within the totally symmetric subspace, as done here, is that one can straightforwardly associate a classical Hamiltonian to the Dicke model in Eq. (7) by employing coherent states. The corresponding classical Hamiltonian h_D is obtained by taking the expectation value of $\hat{H}_D$ under the tensor product of bosonic Glauber $|\beta\rangle$ and atomic Bloch $|w\rangle$ coherent states [48,72–77]

$$|z\rangle = |\beta\rangle \otimes |w\rangle = \frac{e^{-|\beta|^2/2}}{(1+|w|^2)^j} e^{\beta \hat{a}^\dagger} e^{w\hat{J}_+}|0\rangle \otimes |j,-j\rangle, \quad (8)$$

where $|0\rangle$ and $|j,-j\rangle$ are the boson and pseudospin fiducial states, respectively [78]. By dividing over j, we obtain

$$h_D(z) = j^{-1}\langle z|\hat{H}_D|z\rangle = j^{-1}\omega|\beta|^2 - \omega_0\left(\frac{1-|w|^2}{1+|w|^2}\right)$$
$$+ \frac{\Omega(\beta+\beta^*)(w+w^*)}{\sqrt{2j}(1+|w|^2)}. \qquad (9)$$

Changing to canonical variables (x,p) and (ϕ, j_z) in phase space, it reads

$$h_D(z) = \frac{\omega}{2}(x^2+p^2) + \omega_0 j_z + \Omega\sqrt{1-j_z^2}\,x\cos\phi, \qquad (10)$$

where $\beta = \sqrt{j/2}(x+ip)$, $w = \tan(\theta/2)e^{-i\phi}$, $j_z = -\cos\theta$, and $\phi = \tan^{-1}(j_y/j_x)$. While x and p are the classical quadratures of the field, θ and ϕ are the spherical angles of the angular momentum vector $\vec{j} = j(j_x, j_y, j_z)$ lying in the Bloch sphere. Using coherent states, one can establish a direct quantum-classical correspondence, where a given coherent state $|z_0\rangle = |x_0, p_0; \phi_0, j_{z0}\rangle$ represents a point in the classical phase space. We exploit this connection to explore the multifractal properties of the classical phase space from a quantum point of view, much in the sense of what was done for D_2 in Ref. [33].

We work in the parameter space of the superradiant phase. The superradiant quantum phase transition occurs when the Rabi splitting attains the critical value $\Omega_c = \sqrt{\omega\omega_0}$, and the system goes from an uncorrelated, normal phase ($\Omega < \Omega_c$) to a strongly correlated, superradiant phase ($\Omega > \Omega_c$) [79–82]. It has been shown that in the superradiant phase, the spectrum of the model exhibits a transition from regularity to chaos as the energy increases for both the quantum and classical Hamiltonians [48,76]. We set the Rabi splitting to $\Omega = 2.0\Omega_c$, where the regular-to-chaos transition happens smoothly.

IV. MULTIFRACTALITY IN THE DICKE MODEL

The Dicke model is nonintegrable, because it does not possess enough conserved quantities as degrees of freedom, so it must be solved numerically. Due to the bosonic degree of freedom, the Hilbert space is unbounded, which constitutes a significant challenge for the complete analysis of multifractality. To obtain the energy spectrum, one has to impose a cutoff to the bosonic subspace (irrespective of the chosen basis) and then ensure that the eigenfunctions are converged up to the desired energy that one plans to investigate [83,84].

A. Convergence and effective dimension

We use a convergence criterion for $q = 1$ to ensure that most of the wave function of the coherent states that we consider lie within the energy interval of numerically converged eigenstates, ranging from the ground-state to a selected excited energy, so minor components over higher energies remain negligible, and the normalization is guaranteed to a set of significant figures. Nevertheless, minor components associated with high-lying states are magnified and become not negligible for $q \sim 0$. The analysis of multifractality is thus challenging for IPR$_q$ with $q \sim 0$, which are highly sensitive to the convergence of the wave functions and the truncation. In particular, the Hausdorff dimension $D_0 = D$ of the coherent

states can hardly ever be identified for the Dicke model, although it can be estimated for some cases. The convergence problem is minimized by increasing the value of the cutoff, but this becomes highly expensive in terms of computational resources.

The scaling analysis also requires setting a finite, effective dimension $\aleph_{\text{eff}}$ for the coherent states with a given mean energy. A naive choice would be the size of the collective qubit space, which goes as $j = \mathcal{N}/2$. Nevertheless, by studying the participation of states in a given energy surface and considering that the density of states (DoS) scales as j, it was recently shown that the proper scaling should go as $\aleph_{\text{eff}} \sim j^{3/2}$, instead of $\aleph_{\text{eff}} \sim j$ [85]. Therefore, we use $\aleph_{\text{eff}} \sim j^{3/2}$ as the effective size of the Hilbert space to perform the multifractal analysis.

B. Limiting cases of the generalized dimension

To analyze the numerical results, we contrast them with two bounds for the scaling of IPR_q. They are obtained as follows.

(i) First, we consider a state $|\Psi^{(r)}\rangle$ with random components and a Gaussian profile. We can estimate the scaling of IPR_q exactly (see Appendix A),

$$\text{IPR}_q^{(r)} \sim \aleph_{\text{eff}}^{(1-q)}. \tag{11}$$

The mass exponent is linear as a function of q, $\tau_q^{(r)} = q - 1$, and the state is described in terms of a single fractal of dimension $D_q^{(r)} = D = 1$. This corresponds to an extended state and constitutes an overall upper bound of localization of the coherent states in the energy eigenbasis. This bound is indicated with a red dotted line in both Figs. 1 and 2, panels (a2)–(a4) and (b2)–(b4).

(ii) The other bound is obtained with a state $|\Psi^{(c)}\rangle$ for which most of the components in the eigenbasis are zero, except for a single sequence of nearly equally spaced energy levels $\{..., E_k^{(\text{seq})}, E_{k+1}^{(\text{seq})}, ...\}$. We assume that these nonzero components also follow a Gaussian profile. This would be the case of a coherent state centered in a point in phase space over a regular classical orbit with a single frequency $\omega_{\text{cl}} = E_{k+1}^{(\text{seq})} - E_k^{(\text{seq})}$ [86]. As it is shown in Appendix A, one obtains that

$$\text{IPR}_q^{(c)} \sim \aleph_{\text{eff}}^{\frac{1}{3}(1-q)}. \tag{12}$$

This means that $\tau_q^{(c)} = (1/3)(q - 1)$ is also linear and that a single fractal of dimension $D_q^{(c)} = D = 1/3$ can describe the state. This is an overall lower bound for the localization of a coherent state over the eigenbasis (lower bound for D_q). This case is indicated as a blue dotted line in both Figs. 1 and 2, panels (a2)–(a4) and (b2)–(b4). We note that for a Gaussian distribution of a real state, where the components may be small but not exactly zero, the curve of τ_q versus q in the region $0 < q < 1$ deviates from $D = 1/3$. Then, for $q = 0$, all the components have the same weight, and the distribution covers the full available support, so $D_0 = -1$.

We expect the fractal dimension of most coherent states to be in the interval $D_q \in [D_q^{(c)}, D_q^{(r)}]$ when neglecting minor deviations due to finite-size effects and convergence of the wave functions. However, some states may have $D = 0$ for $q > 1$ thus presenting localization features for $q > 1$.
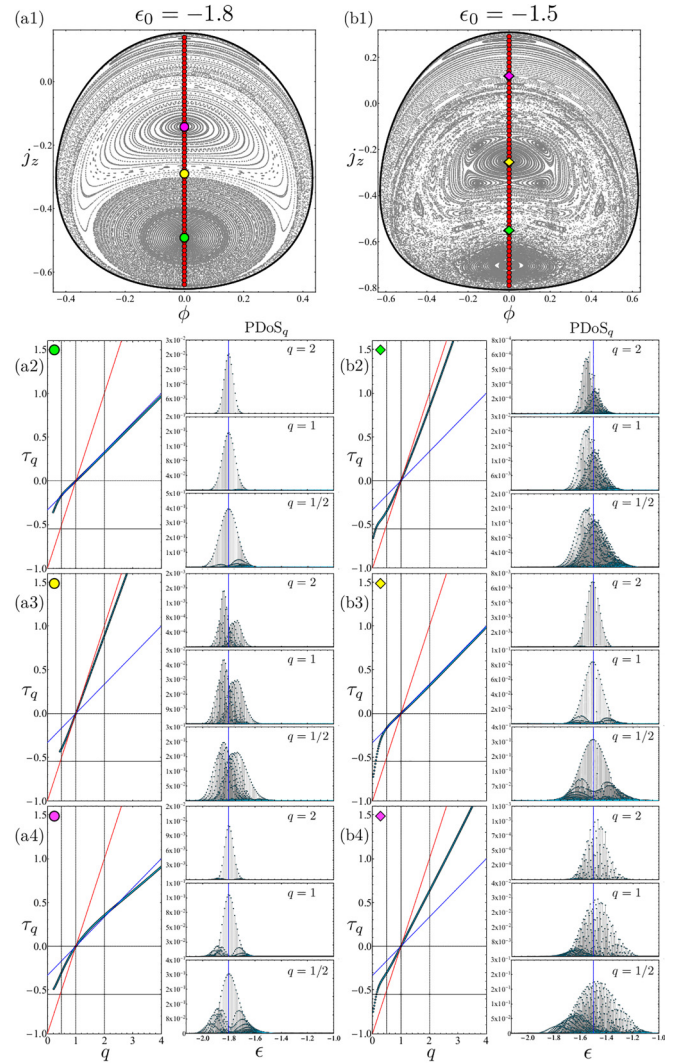

FIG. 1. (Top row) Poincaré surface of sections for two selected energies, $\epsilon_0 = -1.8$ (a1) and $\epsilon_0 = -1.5$ (b1), where there is predominance of regular structures in phase space. (Below) Mass exponents τ_q (first and third columns) as a function of q for selected coherent states in each energy surface, and their PDoS_q (second and fourth columns) for different values of q, and $\epsilon_0 = -1.8$ (a2–a4) or $\epsilon_0 = -1.5$ (b2–b4); $j = 100$ for all panels. The location of each coherent state in the Poincaré surface is marked with a symbol (circles for $\epsilon_0 = -1.8$ and diamonds for $\epsilon_0 = -1.5$). In the τ_q plots, the dotted cyan line corresponds to numerical results, the colored lines indicate the ergodic (red) and regular (blue) limiting cases of the D_q, the vertical black solid lines mark $q = 1/2$, 1, and 2. In the PDoS_q plots, the vertical blue line marks the mean energy.

C. Procedure for the analysis of multifractality

Our procedure to study the multifractal properties of coherent states goes as follows. We select a coherent state $|z_0\rangle$ centered at the point z_0 in phase space. We choose a set of points from an energy surface that coincides with one of the Poincaré surfaces of sections as shown in Figs. 1 and 2, panels (a1) and (b1). The Poincaré sections are chosen by setting $p_0 = 0$ and selecting the positive branch of the solution $x_0^+ = x_0^+(\epsilon_0, p_0 = 0; \phi, j_z)$ that results from solving the equation $h_D(x_0, p_0 = 0; \phi, j_z) = \epsilon_0$ for a given energy $\epsilon_0 = E_0/j$
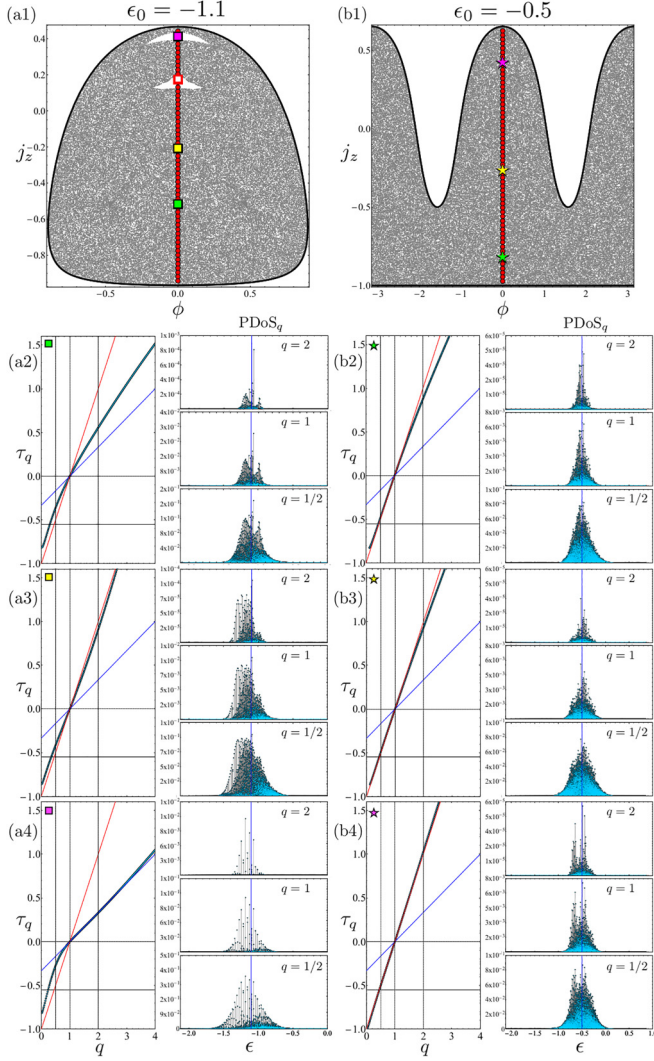
FIG. 2. Similar to Fig. 1 for the two selected energies $\epsilon_0 = -1.1$ (a1) and $\epsilon_0 = -0.5$ (b1), where there is predominance of chaos. Notice the change of scale in panel (b1) due to the sudden increase of available phase space at high energies [74]. The location of each coherent state in the Poincaré surface is marked with a symbol (squares for $\epsilon = -1.1$ and stars for $\epsilon = -0.5$).

[33]. The points in phase space are thus located using only the atomic variables (ϕ, j_z). Next, we sample the energy surface by focusing only on the points along $\phi_0 = 0$ [red points in Figs. 1 and 2, panels (a1) and (b1)].

The surface energies grant insight into different regions of chaos and regularity: for $\epsilon_0 = -1.8$, there is a major presence of regular orbits with chaos emerging in small regions [Fig. 1(a1)]; for $\epsilon_0 = -1.5$ the phase space is mixed [Fig. 1(b1)]; for $\epsilon_0 = -1.1$, there is a predominance of chaos with some remaining regular islands [Fig. 2(a1)]; and at $\epsilon_0 = -0.5$, the system appears to be fully chaotic [Fig. 2(b1)]. Within each energy surface, we choose a set of three representative points marked with colored symbols, whose coordinates j_{z0} are given in Table I.

Then, we solve the Dicke Hamiltonian numerically for several values of j from 5 to 120 ($2j$ qubits) and a cutoff of $n_{\max} = 300$ quanta in the bosonic field to ensure convergence

TABLE I. Values of j_{z0} for twelve representative points in the Poincaré surfaces in Figs. 1 and 2, panels (a1) and (b1). The points are taken with $\phi_0 = 0$, $p_0 = 0$ and the positive branch of the solution for x_0^+ at the corresponding energy ϵ_0.

	$\epsilon_0 = -1.8$				$\epsilon_0 = -1.5$		
	(a2)	(a3)	(a4)		(b2)	(b3)	(b4)
j_{z0}	-0.492	-0.290	-0.143	j_{z0}	-0.548	-0.250	0.123
	$\epsilon_0 = -1.1$				$\epsilon_0 = -0.5$		
	(a2)	(a3)	(a4)		(b2)	(b3)	(b4)
j_{z0}	-0.512	-0.202	0.418	j_{z0}	-0.807	-0.257	0.431

of about 30 000 eigenstates. See Appendix B for a comparison between the truncation for $n_{\max} = 300$ and $n_{\max} = 250$. The first step for our analysis of multifractality is to get the mass exponents. For each j and each coherent state considered, we calculate IPR_q and, according to Eq. (5), obtain τ_q by linearly fitting the logarithmic plot of IPR_q versus $\aleph_{\mathrm{eff}}$, as shown in Figs. 3(a) and 3(b) for two representative coherent states, as examples. To avoid finite-size effects, we ignore the first points (from $j = 5$ to $j = 20$) when performing the fittings in Fig. 3. The results obtained are used in the plots of τ_q versus q shown in Figs. 1(a2)–1(a4), 1(b2)–1(b4) and Figs. 2(a2)–2(a4). These plots are subsequently used to extract the generalized dimensions D_q. To assist our studies of multifractality, we also examine the distribution of the coefficients of each coherent state with respect to energy for a given q, what we call generalized participation local density of states,

$$\mathrm{PDoS}_q(\epsilon) = \sum_k |c_k|^{2q} \delta(\epsilon - \epsilon_k), \qquad (13)$$

where $|c_k|^{2q} = |\langle E_k | z_0 \rangle|^{2q}$, $|E_k\rangle$ are the eigenstates of the Dicke Hamiltonian, and $\epsilon_k = E_k / j$ are the scaled eigenergies. The PDoS_q is related to the generalized local density of states
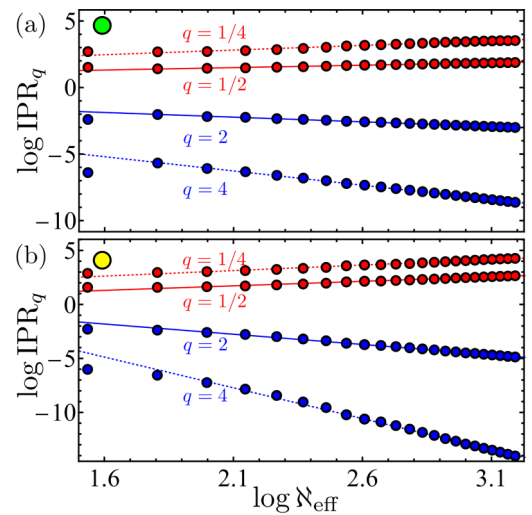

FIG. 3. Logarithmic plot of IPR_q as a function of $j^{3/2}$ ($j = 5$ to 120) for (a) the same coherent state as in Fig. 1(a2) and (b) the same coherent state as in Fig. 1(a3), for $q = 1/4$, $1/2$, 2, and 4. The linear fits ignore the first points, from $j = 5$ to $j = 20$, to avoid finite-size effects.

[87] upon changing $2q$ by q. Plots for the PDoS_q are shown in Figs. 1 and 2. The analysis of PDoS_q for different values of q reveals structures hidden in the coherent states that help us better understand the source of multifractality.

D. Predominance of regularity

We start by analyzing three representative coherent states within a low-energy domain ($\epsilon_0 = -1.8$), where regularity is predominant in phase space.

1. Green circle in Fig. 1(a1)

The green circle in Fig. 1(a1) indicates the center of a coherent state placed near a stable periodic orbit that emanates from a pseudoconserved quantity of the Dicke Hamiltonian [88,89]. This coherent state is mainly described by a subset of nearly equally spaced eigenstates, and its PDoS_q for $q = 1$, shown in Fig. 1(a2), has a Gaussian profile. The shape of PDoS_q for $q > 1$, as illustrated for $q = 2$ also in Fig. 1(a2), remains Gaussian, because small coefficients $|c_k|^{2q}$ become negligible as q increases from 1. Accordingly, the D_q for $q > 1$, obtained using Eq. (2) and the data in Fig. 1(a2), follows almost exactly $D_q^{(c)} = 1/3$.

The result for D_q with $q > 1$ suggests that the coherent state is monofractal. However, for $q < 1$, new structures emerge within the Gaussian envelope of PDoS_q, as seen for $q = 1/2$ in Fig. 1(a2). They are caused by small contributions $|c_k|^{2q}$ that are associated with classical trajectories slightly away from the center of the set of regular orbits in the Poincaré section, which are sampled by the selected coherent state. In turn, this is reflected in the behavior of the mass exponents as a function of q. For $q < 1$, τ_q deviates from the linear behavior, thus suggesting multifractality.

To determine whether the state is then mono- or multifractal, a better picture is achieved by analyzing τ_q versus q for $q < 1$ in Fig. 4(a) and for $q > 1$ in Fig. 4(b). We show in Fig. 4(a) that the linear fitting, given by $\tau_q = \mathcal{D}^{(0)} + \mathcal{D}^{(1)}(q - 1)$ (solid black line), fails to describe the behavior of τ_q around $q \in [0.2, 0.5]$, as it becomes nonlinear when q decreases. Instead, both the parabolic fitting $\tau_q = \mathcal{D}^{(0)} + \mathcal{D}^{(1)}(q - 1) + \mathcal{D}^{(2)}q^2$ (red dashed curve) and the square root $\tau_q = \mathcal{D}^{(0)} + \mathcal{D}^{(1)}(q - 1) + \mathcal{D}^{(1/2)}q^{1/2}$ (blue dashed curve) perform better. Instead, for $q > 1$ in Fig. 4(b), the behavior is mostly linear, being described by the slope $D_q^{(c)} = 1/3$. Thus, the result for $q < 1$ makes it clear that this state is multifractal, and it serves to benchmark the multifractal behavior in the regular region. As we shall see, the nonlinear departure from $D_q^{(c)}$ for $q < 1$ also appears for other coherent states centered in regular regions of the phase space.

2. Yellow circle in Fig. 1(a1)

The coherent state centered at the yellow circle in Fig. 1(a1) is close to the stochastic layer where chaos is emerging [90]. In this case, the PDoS_q for $q = 1$ is made of a set of Gaussians. This feature is invariant and persists for larger or smaller values of q. As a result, the mass exponent in Fig. 1(a3) is basically a straight line leading to a value of D_q very close to the upper bound $D_q^{(r)} = 1$. This implies that this state is not multifractal but an ergodic state.
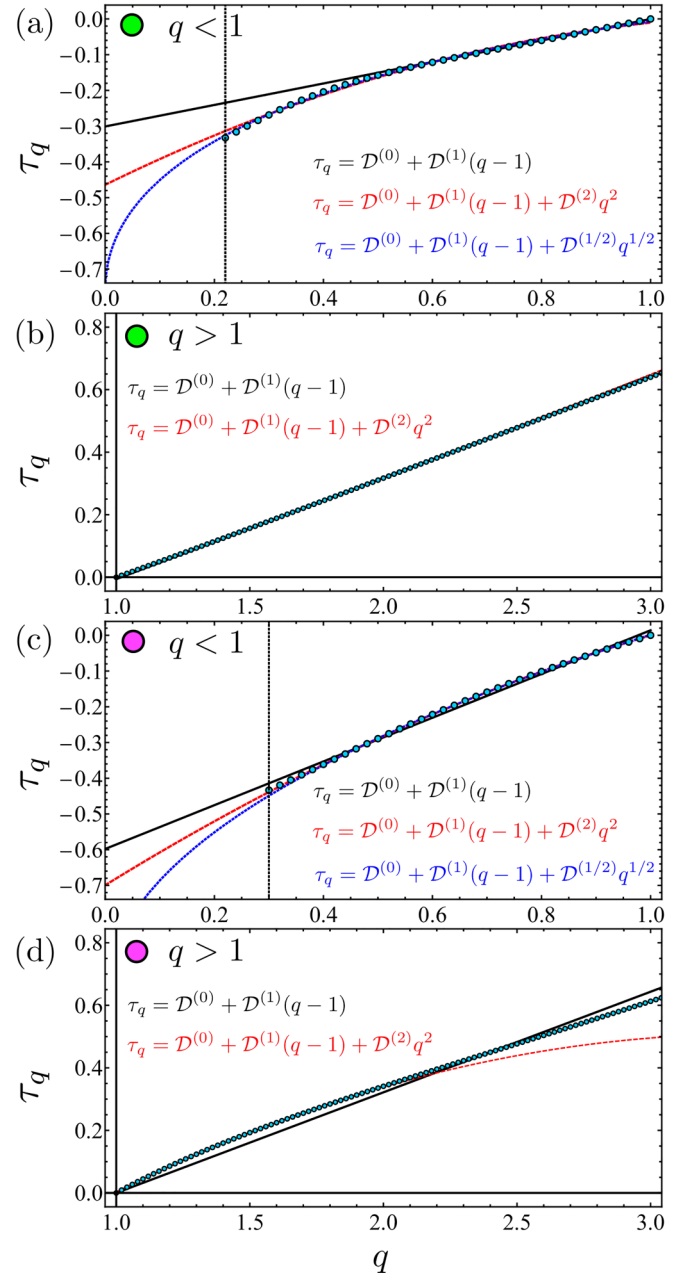

FIG. 4. Mass exponent τ_q (blue dots) as a function of q for the coherent state in Fig. 1(a2) for (a) $q < 1$ and (b) $q > 1$, and for the coherent state in Fig. 1(a4) for (c) $q < 1$ and (d) $q > 1$. Three different fits are shown: linear (solid black line), quadratic (red dashed line), squared root (blue dashed line). The dashed vertical black line represents the lowest value of q where the convergence of the wave function is applicable.

At very small values of $q \ll 1$, there is a change in the curvature of the mass exponent [the beginning of this change is noticeable in Fig. 1(a3)], but this is an artifact caused by the truncation of the Hilbert space. We know this because it gives a positive second derivative of the mass exponent, while this derivative must always be negative [60]. In fact, the point where the curvature of the τ_q becomes positive could be used as an alternative tool to determine the convergence of the wave function. Our current convergence criterion for the

wave functions is established for $q = 1$ to ensure that most of the state is contained within the energy domain of interest [83,84]. It is impossible to guarantee the convergence of the whole wave function unless we set the truncation to infinity. This problem becomes more important for highly extended states. For low energy regimes, such as $\epsilon_0 = -1.8$ and -1.5, the small phase space available is another problem that one needs to keep in mind. In this case, a finite-size effect arises, turning the curvature of τ_q from negative to positive. This effect is a result of the artificial truncation of low-energy states due to the Hilbert space being bounded from below, as can be seen in the PDoS$_q$ in Figs. 1(a2)–1(a4). This finite-size effect can be removed by increasing j, but this requires even larger values of $n_{\max}$ to ensure overall convergence. We must discard any result that gives a positive curvature of τ_q when fitting the curves to get D_q.

3. Magenta circle in Fig. 1(a1)

We now focus on the coherent state centered at the magenta point in the phase space of Fig. 1(a1). The state is inside a regular region but surrounded by regular orbits resulting from a nonlinear resonance that appears in the Dicke Hamiltonian between the two normal modes at low energies [88,89,91]. Like the case of the green circle, for $q = 1$ and $q = 2$, the PDoS$_q$ shows the dominance of a single Gaussian, while for $q = 1/2$, more Gaussians appear. For this state, we see that τ_q is nonlinear not only for $q < 1$, as before, but also for $q > 1$. The slope of the curve for τ_q is close to $D_q^{(c)} = 1/3$, but deviates from it in both limits of q.

We compare the curve for τ_q versus q with different fittings in Fig. 4(c) for $q < 1$ and in Fig. 4(d) for $q > 1$. Unlike the green-circle coherent state in Fig. 4(a), for the magenta-circle coherent state, the quadratic fit for $q < 1$ [Fig. 4(c)] is better than the one that goes as $q^{1/2}$. As we turn to $q > 1$, we see that for $q \gg 1$, a linear fitting seems to be the best one, although for $q \gtrsim 1$, the quadratic fitting describes well the nonlinearity. While both coherent states marked by the green and magenta circles are in a regular region, the magenta one is surrounded by orbits associated with a nonlinear resonance. This may impact the structure of the coherent states and be associated with the multifractal behavior for $q > 1$.

E. Mixture of chaos and regularity

By increasing the energy, we introduce a mixture of chaos and regularity, as shown in Fig. 1(b1) for $\epsilon_0 = -1.5$. For our analysis, we choose three coherent states with this energy and centered at the points marked with diamonds in Fig. 1(b1). The point indicated by a green diamond is away from the three major regular islands and inside an emergent sea of chaos. The coherent state associated with this point shows a behavior similar to that of the yellow circle with $\epsilon_0 = -1.8$ in Fig. 1(a3). The PDoS$_q$ exhibits clustered Gaussians, and τ_q is almost linear with a slope very close to $D_q^{(r)} = 1$, which indicates that this coherent state is ergodic.

The magenta diamond in Fig. 1(b1) is located in a mixed region. Compared with the green-diamond coherent state, the components of the PDoS$_q$ for the magenta-diamond state are less concentrated around the energy of the surface. Even though τ_q presents a linear behavior [see Fig. 1(b4)],
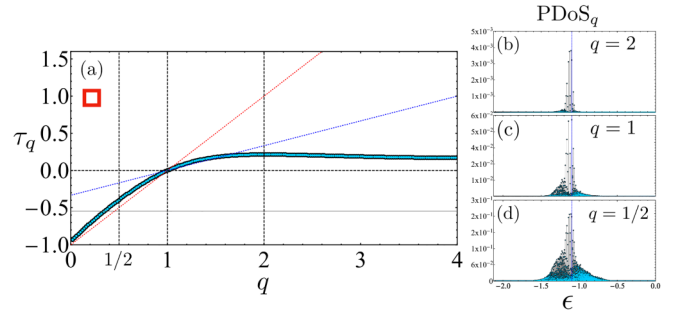

FIG. 5. (a) Mass exponents τ_q as a function of q for the coherent state marked by the white square encircled in red in Fig. 2(a1) at $\epsilon = -1.1$, and PDoS$_q$ for (b) $q = 2$, (c) $q = 1$, and (d) $q = 1/2$.

indicating that the state is monofractal, the extracted value of D_q is between those for a random and a regular state.

The coherent state indicated with the yellow diamond in Fig. 1(b1) lies in a similar position to the magenta circle in Fig. 1(a1), i.e., at the center of the regular island of the nonlinear resonance orbits. While it exhibits nonlinear behavior for $q < 1$ [see Fig. 1(b3)], it shows an almost perfect linear behavior for $q > 1$ with $D_q^{(c)} = 1/3$. Finding linear behaviors like this allows us to use D_q to identify regular regions in phase space.

F. Predominance of chaos

We now explore a higher energy ($\epsilon_0 = -1.1$) in Fig. 2, where chaos is dominant, but some regions of regularity still exist. The first coherent state that we select is amidst the chaotic sea and is marked with a green square in Fig. 2(a1). The components of the PDoS$_q$ next to Fig. 2(a2) are randomly distributed, but some regular structures can still be identified. Hence, we obtain a slope for the τ_q curve that is between $D_q^{(c)}$ and $D_q^{(r)}$, similarly to the coherent state marked with the magenta diamond in Fig. 1(b4).

In contrast to the above, the coherent state marked with the yellow square in Fig. 2(a3) is fully extended. This is not obvious from the PDoS$_q$, as it seems to be shaped by two Gaussians for $q = 1$. Instead, when we go to $q < 1$, all the Gaussians seem to have comparable weight. The ergodic nature of the state gets determined from the slope of the τ_q, which is constant and equal to $D_q^{(r)} = 1$.

Moving to larger values of j_z in the Poincaré section of Fig. 2(a1), we reach the magenta square, which is at a regular island. The slope of the curve for τ_q in Fig. 2(a4) is close to $D_q^{(c)} = 1/3$, confirming that the state is regular. This means that by studying the behavior of the mass exponents, we can locate regular regions even in very chaotic domains.

In Fig. 2(a1), we identify another regular coherent state with special behavior. It is located in the other stability island in Fig. 2(a1) and is marked with a white square encircled in red. The behavior of τ_q for this coherent state is shown in Fig. 5(a). It presents a highly nonlinear behavior for $q < 2$, while τ_q becomes nearly flat for $q > 2$. This indicates that this state has an effective dimension of $D_\infty \simeq 0$. This is confirmed by looking at the PDoS$_q$ in Fig. 5(b). We see in Figs. 5(b)–5(d) that as q increases from $q = 1/2$ to $q = 2$, the number of

components relevant to describe the state decreases quickly, in agreement with the idea that when $D_q = 0$, we have a state with zero measure in the Hilbert space. However, for $q < 1$, we see in Fig. 5(a) that D_q follows the behavior of an ergodic state with $D_q^{(r)}$, which is also suggested by the PDoS$_q$ in Fig. 5(d). This state is of particular interest because it exhibits a highly multifractal behavior. For $q < 1$, it behaves as a Gaussian state, while for $q > 1$, D_∞ tends to 0. Although the phase space might look qualitatively similar in the Poincaré section, the multifractal method unveils quantitative differences between this coherent state and that marked by the magenta square at the same energy but in another regular zone [see Fig. 2(a4)]. Because of the resolution limits imposed by the numerical diagonalization, a supplementary approach as a dynamical tool, such as the survival probability [86] or out-of-time ordered correlators [92], could help to understand the details of the participating structures and unveil the reasons behind the observed multifractal behavior.

In Fig. 2(b1), we consider an even higher energy ($\epsilon_0 = -0.5$), where one expects ergodic behavior [48,93]. The three selected coherent states are centered at the points labeled by stars. As shown in Figs. 2(b2)–2(b4), they are not multifractal but just single fractals with an approximated dimension close to $D_q^{(r)} = 1$, indicating ergodicity. The different shape of the phase space happens because the two wells at low energies in the energy surface of the Dicke model merge together [74].

V. FRACTAL DIMENSION OVER ENERGY SURFACES

Now that the detailed study of representative coherent states is complete, we proceed to build a general characterization of the energy surfaces through the information stored in the mass exponents. To this end, we fit the curve for τ_q versus q with the parabolic approximation $\tau_q = \mathcal{D}^{(0)} + \mathcal{D}^{(1)}(q - 1) + \mathcal{D}^{(2)}q^2$. This way, we can extract the linear part of the fit, $\mathcal{D}^{(1)}$, and use it as a probe to determine whether the state is ergodic ($\mathcal{D}^{(1)} = D_q^{(r)} = 1$), regular ($\mathcal{D}^{(1)} = D_q^{(c)} = 1/3$), localized ($\mathcal{D}^{(1)} = D_q = 0$), or anything in between. We can also obtain the quadratic part, $\mathcal{D}^{(2)}$, and use it as a first-order measure of the nonlinear behavior of the state, hence the presence of multifractality. For our analysis, we study the sample of points over the Poincaré surface of sections with $\phi_0 = 0$ marked in Figs. 1 and 2, panels (a1) and (b1).

The linear part of the fit $\mathcal{D}^{(1)}$ is used to approximate the linear part of the generalized dimension D fitted over the $q > 1$ domain. We investigate $\mathcal{D}^{(2)}q^2$ for both $q < 1$ and $q > 1$ to estimate the departure from the linear behavior quantified by Δ.

A. Ergodic versus multifractal coherent states

We first use the parabolic approximation to fit the mass exponents for $q > 1$, in the region $q \in [1, 2]$ and focus on the analysis of the linear approximation characterized by $\mathcal{D}^{(1)}$. Under the weak multifractality approximation, as discussed in the context of Eq. (6), the coefficient to the linear part should formally be $\mathcal{D}^{(1)} = D + \Delta$. However, as the parabolic approximation does not hold systematically over the whole phase space, we work under the approximation that $\mathcal{D}^{(1)} \simeq D$ for $q > 1$.
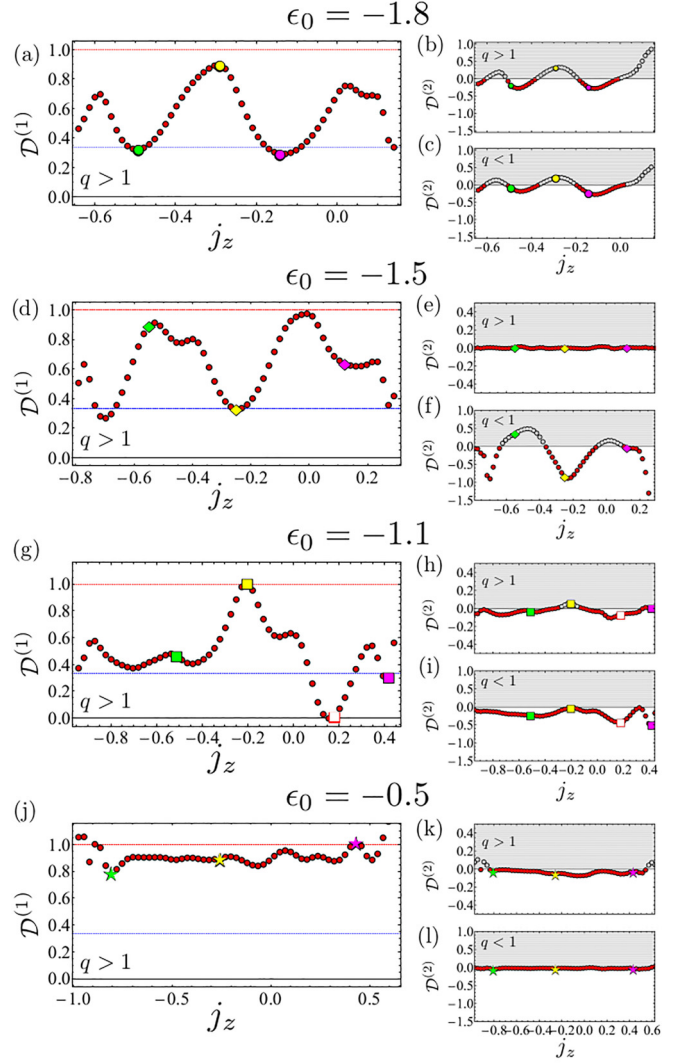

FIG. 6. Linear approximation to the generalized dimension $\mathcal{D}^{(1)}$ as a function of j_z with $\phi = 0$ over the energy surface for (a) $\epsilon_0 = -1.8$, (d) $\epsilon_0 = -1.5$, (g) $\epsilon_0 = -1.1$, and (j) $\epsilon_0 = -0.5$. Parabolic approximation to the anomalous fractal dimensions $\mathcal{D}^{(2)}$ over the same energy surfaces for $q > 1$ (b, e, h, k) and $q < 1$ (c, f, i, l). The region in gray indicates the points that should not be considered, as $\mathcal{D}^{(2)}$ becomes positive.

Our results for $\mathcal{D}^{(1)}$ as a function of j_z are shown in Figs. 6(a), 6(d) 6(g), and 6(j) for the energy surfaces studied in Figs. 1 and 2. For the surface with $\epsilon_0 = -1.8$ [Fig. 6(a)], where regularity dominates, $\mathcal{D}^{(1)}$ locates the regular regions around $j_z \sim -0.5$, $j_z \sim -0.2$, and $j_z \sim 0.1$, where $\mathcal{D}^{(1)} \sim 1/3$. Notice that the lowest value of $\mathcal{D}^{(1)}$ for this energy surface with $\epsilon_0 = -1.8$ is $D_q^{(c)}$, so there are no states with features of localization, that is, $\mathcal{D}^{(1)}$ is never close to zero. The value of $\mathcal{D}^{(1)}$ in Fig. 6(a) also detects the emergence of chaos. Even though it does not reach $D_q^{(r)}$, it does capture significantly extended states around $j_z \sim -0.3$, where the stochastic layer is developing.

In the mixed region at $\epsilon_0 = -1.5$ [Fig. 6(d)], $\mathcal{D}^{(1)}$ again detects regular and chaotic regions. For $j_z \sim 0.0$, $\mathcal{D}^{(1)}$ now reaches $D_q^{(r)}$, indicating the presence of ergodic states and thus of fully chaotic regions.

The most interesting results appear at the energy surface $\epsilon_0 = -1.1$ [Fig. 6(g)], where chaos has developed, and only a few regular domains survive in phase space. This figure makes it evident that the linear approximation to the fractal dimension $\mathcal{D}^{(1)}$ provides more detail about the phase space than the Poincaré section. While the latter suggests that most of the phase space is fully chaotic, $\mathcal{D}^{(1)}$ shows that only the states around $j_z \sim -0.2$ are fully extended, having $\mathcal{D}^{(1)} \sim D_q^{(r)} = 1$. As we move away from this point, towards larger values of j_z, there is an abrupt decrease in the values $\mathcal{D}^{(1)}$ until it reaches $\mathcal{D}^{(1)} = 0$ around $j_z \simeq 0.1$, indicating that we have found a state with localized features for $q > 1$. If instead we move away from $j_z \sim -0.2$, towards smaller values of j_z, then we see that for the coherent states with $j_z < -0.4$, $\mathcal{D}^{(1)}$ has values similar to those seen for surfaces with low energies, getting close to $D_q^{(c)} = 1/3$. This implies that energy surfaces with qualitatively different phase space structures may actually have similar values of the approximated fractal dimension.

For the energy surface at high energy, $\epsilon_0 = -0.5$ in Fig. 6(j), we expect ergodic behavior. Indeed, over the whole energy surface, $\mathcal{D}^{(1)} \sim D_q^{(r)} = 1$. This analysis demonstrates that $D = \mathcal{D}^{(1)}$, despite belonging to the quantum world, is a good quantity to probe chaos and regularity in phase space, and to uncover its structures.

B. Multifractal versus fractal coherent states

The approximated linear fractal dimension, $D \simeq \mathcal{D}^{(1)}$, allows for the quantitative classification of the coherent states into ergodic, regular, or an intermediate fractal case. However, it only reveals single fractal behavior. Extended states that are neither ergodic ($D_q = 1$) nor regular ($D_q = 1/3$) can be mono- or multifractal. To quantify multifractality and distinguish between mono- and multifractal states, we need to study the deviations from linear behavior. For this, we look at the quadratic order of the fitting curve for the mass exponents, $\tau_q = \mathcal{D}^{(0)} + \mathcal{D}^{(1)}(q-1) + \mathcal{D}^{(2)}q^2$, for both $1 \leqslant q \leqslant 2$ and $0.3 \leqslant q \leqslant 1$. If the value of the quadratic term in the fractal dimension $\mathcal{D}^{(2)}$ is different from zero and negative, then the mass exponent has a nonlinear behavior of the order of weak multifractality. It is worth emphasizing that the quadratic fit is not general, as the anomalous fractal dimension Δ_q could be an arbitrary function of q (under the curvature constraints for τ_q). Yet, we choose the quadratic fitting as a general way to detect nonlinearity, so when the behavior is parabolic $\mathcal{D}^{(2)} \simeq \Delta$.

At the energy surfaces $\epsilon_0 = -1.8$ [Figs. 6(b) and 6(c)] and $\epsilon_0 = -1.1$ [Fig. 6(h) and 6(i)], we observe that for $q > 1$, most states have $\mathcal{D}^{(2)} \sim 0$, except those around the regular islands. In this case, there is a slight decrease in the value of $\mathcal{D}^{(2)}$ indicating the multifractal nature of those states. The same happens for $q < 1$, where $\mathcal{D}^{(2)}$ signals nonlinear behavior and weak multifractality around the regular islands. Notice that $\mathcal{D}^{(2)}$ becomes positive for some states, typically the most extended ones. This is an artifact caused by the combination of the already mentioned finite-size effects at low energies and the limitations of the wave-function convergence. Since Δ must always be negative, any value of $\mathcal{D}^{(2)}$ different from zero but positive must be discarded. The region

where the points need to be discarded is indicated in gray in Figs. 6(a)–6(l).

Nonlinearity is more visible for $q < 1$ when $\epsilon_0 = -1.5$ [Fig. 6(f)]. One sees large oscillations in the values of $\mathcal{D}^{(2)}$. In contrast, for $\epsilon_0 = -0.5$ in Figs. 6(k) and 6(l), we confirm that the system mainly comprises ergodic states.

In general, we conjecture that structural changes in phase space from an extended region to a very localized region, as it occurs for the $D^{(1)}$ at $\epsilon_0 = -1.5$ [Fig. 6(g)], produce significant multifractal behavior, which is identifiable for $\mathcal{D}^{(2)}$ and $q > 1$ [Fig. 6(i)]. From the three energy cases in Fig. 6, $\epsilon_0 = -1.8, -1.5, -1.1$, it seems that the coherent states have to gain a multifractal character across the phase space as they transit from ergodicity to regularity or $D = 0$.

A systematic study of nonlinearities as one moves through phase space is complicated. For example, we showed in Fig. 4(a) that the coherent state marked by the green circle in Fig. 1(a1) at $\epsilon_0 = -1.8$ is better fitted by a curve of the form $\tau_q = \mathcal{D}^{(0)} + \mathcal{D}^{(1)}(q-1) + \mathcal{D}^{(1/2)}q^{1/2}$ for $q < 1$, so a detailed analysis to determine the true multifractal nature of a coherent state must be done individually. Nevertheless, our analysis in this section has demonstrated that the approximation $\mathcal{D}^{(2)} \simeq \Delta$ is enough for a coarse-grained distinction between monofractal and multifractal states.

VI. CONCLUSIONS AND PERSPECTIVES

We have analyzed the fractal properties of coherent states projected in the energy eigenbasis of the Dicke Hamiltonian. The motivation to explore multifractality in this model comes from its experimental accessibility, its well-defined classical limit, and the fact that it represents many-body systems with collective interactions and only two degrees of freedom, which simplifies the description. However, the model has an unbounded Hilbert space, which makes the study of multifractality based on scaling analysis challenging. To obtain the spectrum numerically, one must choose a cutoff of the bosonic space large enough to ensure convergence of the high-energy eigenstates. We used cutoff values that were large enough to ensure the normalization of the wave functions and the accurate computation of the generalized inverse participation ratio with $q > 1$, but nonconverged components still impact the multifractal analysis when one goes to small values of q. We have circumvented this problem by restricting our study to certain ranges of q values.

Although the multifractal analysis has been used before as a probe of ergodicity, here our aim was to employ it as a coarse-grained quantitative tool to capture changes in the structures in a mixed phase space. The multifractal analysis of coherent states reveals details of the rich phase space of the Dicke model and provides a quantitative picture of its structure. We have obtained two main results by studying the mass exponents τ_q.

First, by fitting the curves of τ_q versus q, we verified that the approximation to the linear generalized dimension, $\mathcal{D}^{(1)} \simeq D$, is a valuable tool to distinguish regular from chaotic regions, similar to what was done for the kicked top model in Ref. [32] using D_1, D_2 and D_∞, and for the Dicke model using D_2 [33,89]. The value of D operates as a sensitive probe of the phase space that allows for the identification of chaotic states

in regular regions and regular states associated with islands of stability in the chaotic regime.

Second, we showed that the parabolic correction, $\mathcal{D}^{(2)} \simeq \Delta$, to the linear fit of the mass exponents works as a probe of nonlinearity and thus reveals the presence of multifractal coherent states. We emphasize that states whose linear fractal dimension D is constant and between $D_q^{(r)}$ (ergodic) and $D_q = 0$ (fully localized) are nonergodic extended states that are fractal, but not necessarily multifractal. For multifractality to hold, D_q needs to show a nonlinear behavior with q, which can be detected with the analysis of $\mathcal{D}^{(2)}$.

The multifractal analysis unveils the presence of nonlinearities in the quantum states. From the quantum-classical correspondence, we know that the coherent state samples the vicinity of the phase space around its center, so the presence of multifractality must be a reflection of neighboring hidden structures in the phase space, hinted by the examination of the PDoS$_q$. Multifractality is thus related to dramatic changes in phase space and to the simultaneous participation of different phase space structures.

Moreover, multifractality in the sense of nonergodic extended states was recently studied in the Tavis-Cummings model, an integrable limit of the Dicke model [50]. Alongside our results in the regular region of the Dicke model and those in Ref. [94], it is clear that regular systems can also exhibit multifractality. We leave for a future work, the analysis of how the multifractality of coherent states over the energy eigenbasis gets manifested at the level of classical dynamics. Likewise, recently, there has been an active interest in developing dynamic quantifiers of chaos, including the survival probability for a nonstationary state after a quantum quench [77,86,87,95], or the different out-of-time-ordered correlators (OTOCs) [96,97]. Most of these indicators require information on the eigenfunctions of the Hamiltonian to calculate the dynamics. We deem the multifractal analysis as a complementary approach to these dynamical indicators, and future work will be devoted to understanding more about the phase space structures participating in each coherent state. We hope that the results of our work will motivate the study of multifractality in other systems with bounded and unbounded Hilbert spaces.

Measuring experimental signatures of multifractality in quantum systems has remained elusive to date. Some progress has been made with cold atoms [98–100], disordered conductors [101], and open three-dimensional elastic networks [102]. Three conditions are necessary to detect quantum multifractal features: the ability to measure the wave function in the chosen basis, scalability, and robustness against perturbations [24,25]. For our scheme of coherent states in the Dicke model, we believe that ion trap platforms may offer a good route to explore multifractal signatures [43,44,103], because of its scalability [104] and the possibility of exploring a wide range of Hamiltonian parameters [105]. In these experiments, the spin degree of freedom is encoded in two internal states of the ions, and the boson is realized through the collective center-of-mass motional mode of the ion crystal. While it is currently possible to prepare the system in low-lying states, the challenge would be to prepare it in a high-lying energy coherent state. Another possible approach to extract multifractal information via quantum simulation is to employ the quan-

tum wavelet transform, given that the Dicke model and the coherent states could be efficiently simulated on a quantum computer [106].

APPENDIX A: SCALING OF TYPICAL STATES

In this Appendix we calculate the two bounds for the scaling of the IPR$_q$ discussed in the main text.

1. Scaling of random state with Gaussian profile

We consider a state that has a Gaussian distribution over the eigenbasis with random coefficients,

$$\left| c_k^{(r)} \right|^2 = \frac{r_k}{\sum_k \exp\left(-\frac{(E_k - \bar{E})}{2\sigma_r^2}\right)} \exp\left(-\frac{(E_k - \bar{E})}{2\sigma_r^2}\right), \quad \text{(A1)}$$

where r_k is a random number, $\bar{E}$ is the average energy of the state, and the variance σ_r is chosen arbitrarily. When the dimension of the system grows, i.e., in the limit $j \gg 1$, we approximate the sum by an integral

$$\sum_k \exp\left(-\frac{(E_k - \bar{E})^2}{2\sigma_r^2}\right)$$

$$= \frac{1}{\Delta E} \sum_k {}' \exp\left(-\frac{(E_k - \bar{E})^2}{2\sigma_r^2}\right) \Delta E$$

$$\simeq \bar{\nu} \int \exp\left(-\frac{(E - \bar{E})^2}{2\sigma_r^2}\right) dE = \bar{\nu} \sqrt{2\pi} \sigma_r, \quad \text{(A2)}$$

where $\bar{\nu}$ is the average density of states around the energy window. Therefore,

$$\left| c_k^{(r)} \right|^2 = \frac{r_k}{\sqrt{2\pi}\sigma_r \bar{\nu}} \exp\left(-\frac{(E_k - \bar{E})^2}{2\sigma_r^2}\right). \quad \text{(A3)}$$

Now, we calculate the IPR$_q$,

$$\text{IPR}_q^{(r)} = \sum_k \left| c_k^{(r)} \right|^{2q} = \sum_k \left(\frac{r_k}{\sqrt{2\pi}\sigma_r \bar{\nu}} \exp\left(-\frac{(E_k - \bar{E})^2}{2\sigma_r^2}\right) \right)^q$$

$$= \frac{1}{(\sqrt{2\pi}\sigma_r \bar{\nu})^q} \sum_k r_k^q \exp\left(-\frac{(E_k - \bar{E})^2}{2\sigma_r^2} q\right)$$

$$= \frac{\bar{\nu}}{(\sqrt{2\pi}\sigma_r \bar{\nu})^q} \int r^q(E) \exp\left(-\frac{(E - \bar{E})^2}{2\sigma_r^2} q\right) dE$$

$$= \frac{1}{(\sqrt{2\pi}\sigma_r \bar{\nu})^q} \bar{\nu} \bar{r}^q \sqrt{\frac{2\pi}{q}} \sigma_r$$

$$= \left[\frac{(2\pi)^{(1-q)}}{q} \right]^{1/2} \bar{r}^q (\sigma_r \bar{\nu})^{1-q}. \quad \text{(A4)}$$

The random state samples all the energies present in the energy window, and $\bar{\nu} \sim \nu_0 j$ [74]. Additionally, we chose σ_r corresponding to a coherent states, which scales as $\sigma_r \sim j^{1/2}$ [107]. Then, the scaling of the generalized inverse participation ratios, in this case, is

$$\text{IPR}_q^{(r)} \propto j^{(3/2)(1-q)}. \quad \text{(A5)}$$

Then, for a random state with a Gaussian profile, we have a similar result as that of an ergodic (extended) case, where $D_q = 1$ for all values of q.

2. Scaling of a regular state

Let us now consider the limiting case when a coherent state is centered in a point in phase space just in the center of an island of regularity. As shown in Ref. [86], in this case the coherent state spanned over the eigenbasis has only main contributions from a subset of energy levels, which form a sequence of nearly equally spaced energies, $\Delta E_k^{(\text{seq})} = E_{k+1}^{(\text{seq})} - E_k^{(\text{seq})} \xrightarrow{j \to \infty} \omega_{\text{cl}}$, where ω_{cl} is a finite value, corresponding to the classical frequency of the classical mode activated in the center of the stability island. The squared magnitude of the sequence coefficients of this state are also described by a Gaussian profile,

$$\left| c_k^{(\text{seq})} \right|^2 = \frac{1}{\sum_k \exp\left(-\frac{E_k^{(\text{seq})} - \bar{E}}{2\sigma_c^2}\right)} \exp\left(-\frac{E_k^{(\text{seq})} - \bar{E}}{2\sigma_c^2}\right), \quad \text{(A6)}$$

where σ_c is the variance of the Gaussian profile over the single contributing eigenenergy sequence. By following a similar procedure to that yielding Eq. (A4), we obtain now

$$\text{IPR}_q^{(c)} = \sqrt{\frac{(2\pi)^{(1-q)}}{q}} (\sigma_c \bar{\nu}_c)^{1-q}. \quad \text{(A7)}$$

However, unlike the previous case, $\bar{\nu}_c$ is not the total density of states, but the density of states of the participating sequence of eigenstates, which is given by $\bar{\nu}_c = 1/\Delta E_k^{(\text{seq})}$ and tends to a finite value for large j,

$$\bar{\nu}_c \xrightarrow{j \to \infty} \frac{1}{\omega_{\text{cl}}}.$$

Conversely, as before, $\sigma_c \sim j^{1/2}$ because it comes from a coherent state [86,107]. In this way, the scaling of the $\text{IPR}_q^{(c)}$ is

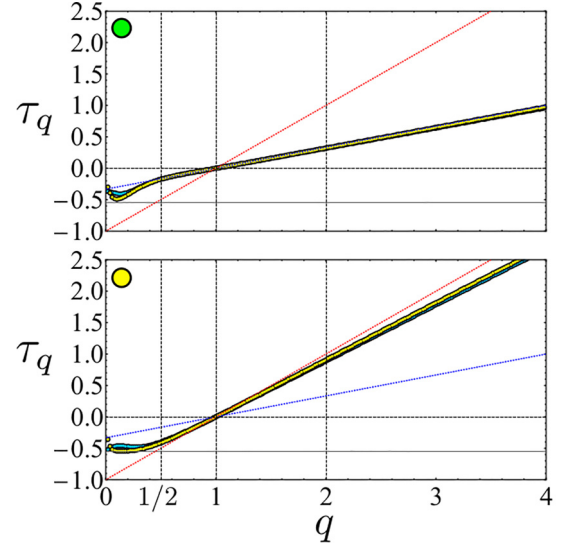$$\text{IPR}_q^{(c)} \sim j^{(1/2)(1-q)} = [j^{(3/2)}]^{1/3(1-q)}. \quad \text{(A8)}$$

FIG. 7. Comparison between the mass exponents τ_q for the respective coherent states in Figs. 1(a2) and 1(a3) at $\epsilon_0 = -1.8$. The data was adjusted for $j = 5$ to 100 and two values of the cutoff: $n_{\max} = 250$ (yellow dots) and $n_{\max} = 300$ (blue dots).

Therefore, for this ideal case where the components out of the main sequence are strictly zero, we get $D_q^{(c)} = 1/3$ for the generalized dimension. However, for the coherent states in the center of the island of stability considered in the main text, the components out of the main sequences are much smaller, but not zero. As a consequence, in the limit of $q \to 0$ the generalized dimension should tend to the maximum value in the space, i.e., $D_{q\to 0} = 1$. This explains why some coherent states around stable points have curvature for $q \ll 1$. Also, this result shows that a Gaussian state possesses an intrinsic multifractal effect as the D_q must go from $1/3$ to 1 as q decreases. This is not a finite-size effect.

APPENDIX B: INCREASING EIGENSTATE CONVERGENCE

In Fig. 7, we show the results that we obtain by decreasing the cutoff over the bosonic Hilbert space of the Dicke model from the value used in the main text $n_{\max} = 300$ (blue dots) to $n_{\max} = 250$ (yellow dots). We employ the same representative points in phase space that are used in Figs. 1(a2) and 1(a3) at the energy surface to $\epsilon_0 = -1.8$. We observe that the results are robust and only slightly deviate for large values of q. The main difference appears for $q < 1$. For $n_{\max} = 300$, the change in the slope for $q < 1$ signaling the limits on the convergence of the wave function occurs for smaller values of q than for $n_{\max} = 250$, although this is hardly noticeable in the figure. The distinction between the two curves becomes visible only for very small values of q.

[1] B. B. Mandelbrot, Intermittent turbulence in self-similar cascades: Divergence of high moments and dimension of the carrier, J. Fluid Mech. **62**, 331 (1974).

[2] P. Grassberger and I. Procaccia, Characterization of strange attractors, Phys. Rev. Lett. **50**, 346 (1983).

[3] P. Grassberger and I. Procaccia, Dimensions and entropies of strange attractors from a fluctuating dynamics approach, Physica D **13**, 34 (1984).

[4] C. Grebogi, E. Ott, and J. A. Yorke, Unstable periodic orbits and the dimensions of multifractal chaotic attractors, Phys. Rev. A **37**, 1711 (1988).

[5] W. G. Hanan and D. M. Heffernan, Multifractal analysis of the branch structure of diffusion-limited aggregates, Phys. Rev. E **85**, 021407 (2012).

[6] P. C. Ivanov, L. A. N. Amaral, A. L. Goldberger, S. Havlin, M. G. Rosenblum, Z. R. Struzik, and H. E. Stanley, Multifractality in human heartbeat dynamics, Nature (London) **399**, 461 (1999).

[7] D. La Rocca, N. Zilber, P. Abry, V. van Wassenhove, and P. Ciuciu, Self-similarity and multifractality in human brain activity: A wavelet-based analysis of scale-free brain dynamics, J. Neurosci. Methods **309**, 175 (2018).

[8] A. D. Mirlin, Y. V. Fyodorov, A. Mildenberger, and F. Evers, Exact relations between multifractal exponents at the Anderson transition, Phys. Rev. Lett. **97**, 046803 (2006).

[9] L. J. Vasquez, A. Rodriguez, and R. A. Römer, Multifractal analysis of the metal-insulator transition in the three-dimensional Anderson model. I. Symmetry relation under typical averaging, Phys. Rev. B **78**, 195106 (2008).

[10] A. Rodriguez, L. J. Vasquez, and R. A. Römer, Multifractal analysis of the metal-insulator transition in the three-dimensional Anderson model. II. Symmetry relation under ensemble averaging, Phys. Rev. B **78**, 195107 (2008).

[11] A. Rodriguez, L. J. Vasquez, K. Slevin, and R. A. Römer, Multifractal finite-size scaling and universality at the Anderson transition, Phys. Rev. B **84**, 134209 (2011).

[12] A. D. Luca and A. Scardicchio, Ergodicity breaking in a model showing many-body localization, Europhys. Lett. **101**, 37003 (2013).

[13] E. J. Torres-Herrera and L. F. Santos, Dynamics at the many-body localization transition, Phys. Rev. B **92**, 014208 (2015).

[14] C. Monthus, Many-body-localization transition: Strong multifractality spectrum for matrix elements of local operators, J. Stat. Mech. (2016) 073301.

[15] A. Solórzano, L. F. Santos, and E. J. Torres-Herrera, Multifractality and self-averaging at the many-body localization transition, Phys. Rev. Res. **3**, L032030 (2021).

[16] J. Lindinger, A. Buchleitner, and A. Rodríguez, Many-body multifractality throughout bosonic superfluid and Mott insulator phases, Phys. Rev. Lett. **122**, 106603 (2019).

[17] M. Pino, V. E. Kravtsov, B. L. Altshuler, and L. B. Ioffe, Multifractal metal in a disordered Josephson junctions array, Phys. Rev. B **96**, 214205 (2017).

[18] S. Sinha and S. Sinha, Chaos and quantum scars in Bose-Josephson junction coupled to a bosonic mode, Phys. Rev. Lett. **125**, 134101 (2020).

[19] S. Roy, I. M. Khaymovich, A. Das, and R. Moessner, Multifractality without fine-tuning in a Floquet quasiperiodic chain, SciPost Phys. **4**, 025 (2018).

[20] M. Sarkar, R. Ghosh, A. Sen, and K. Sengupta, Mobility edge and multifractality in a periodically driven Aubry-André model, Phys. Rev. B **103**, 184309 (2021).

[21] M. Sarkar, R. Ghosh, A. Sen, and K. Sengupta, Signatures of multifractality in a periodically driven interacting Aubry-André model, Phys. Rev. B **105**, 024301 (2022).

[22] D. J. Luitz, F. Alet, and N. Laflorencie, Universal behavior beyond multifractality in quantum many-body systems, Phys. Rev. Lett. **112**, 057203 (2014).

[23] J. Martin, I. García-Mata, O. Giraud, and B. Georgeot, Multifractal wave functions of simple quantum maps, Phys. Rev. E **82**, 046206 (2010).

[24] R. Dubertrand, I. García-Mata, B. Georgeot, O. Giraud, G. Lemarié, and J. Martin, Two scenarios for quantum multifractality breakdown, Phys. Rev. Lett. **112**, 234101 (2014).

[25] R. Dubertrand, I. García-Mata, B. Georgeot, O. Giraud, G. Lemarié, and J. Martin, Multifractality of quantum wave functions in the presence of perturbations, Phys. Rev. E **92**, 032914 (2015).

[26] A. M. Bilen, I. García-Mata, B. Georgeot, and O. Giraud, Multifractality of open quantum systems, Phys. Rev. E **100**, 032223 (2019).

[27] N. Meenakshisundaram and A. Lakshminarayan, Multifractal eigenstates of quantum chaos and the Thue-Morse sequence, Phys. Rev. E **71**, 065303(R) (2005).

[28] V. N. Smelyanskiy, K. Kechedzhi, S. Boixo, S. V. Isakov, H. Neven, and B. Altshuler, Nonergodic delocalized states for efficient population transfer within a narrow band of the energy landscape, Phys. Rev. X **10**, 011017 (2020).

[29] A. D. Mirlin, Statistics of energy levels and eigenfunctions in disordered systems, Phys. Rep. **326**, 259 (2000).

[30] T. Nakayama and K. Yakubo, *Fractal Concepts in Condensed Matter Physics*, 2nd ed., Springer Series in Solid-State Sciences Vol. 140 (Springer, Berlin, 2003)

[31] M. K. Fritz Haake, Sven Gnutzmann, *Quantum Signatures of Chaos* (Springer-Verlag, Berlin, 2018).

[32] Q. Wang and M. Robnik, Multifractality in quasienergy space of coherent states as a signature of quantum chaos, Entropy **23**, 1347 (2021).

[33] M. A. Bastarrachea-Magnani, B. López-del-Carpio, J. Chávez-Carlos, S. Lerma-Hernández, and J. G. Hirsch, Delocalization and quantum chaos in atom-field systems, Phys. Rev. E **93**, 022215 (2016).

[34] R. H. Dicke, Coherence in spontaneous radiation processes, Phys. Rev. **93**, 99 (1954).

[35] B. M. Garraway, The Dicke model in quantum optics: Dicke model revisited, Philos. Trans. R. Soc. A **369**, 1137 (2011).

[36] P. Kirton, M. M. Roses, J. Keeling, and E. G. Dalla Torre, Introduction to the Dicke model: From equilibrium to nonequilibrium, and vice versa, Adv. Quantum Technol. **2**, 1800043 (2019).

[37] J. Larson and T. Mavrogordatos, *The Jaynes–Cummings Model and Its Descendants* (IOP Publishing, Bristol, UK, 2021).

[38] O. Chelpanova, A. Lerose, S. Zhang, I. Carusotto, Y. Tserkovnyak, and J. Marino, Intertwining of lasing and superradiance under spintronic pumping, Phys. Rev. B **108**, 104302 (2023).

[39] K. Baumann, C. Guerlin, F. Brennecke, and T. Esslinger, Dicke quantum phase transition with a superfluid gas in an optical cavity, Nature (London) **464**, 1301 (2010).

[40] K. Baumann, R. Mottl, F. Brennecke, and T. Esslinger, Exploring symmetry breaking at the Dicke quantum phase transition, Phys. Rev. Lett. **107**, 140402 (2011).

[41] H. Ritsch, P. Domokos, F. Brennecke, and T. Esslinger, Cold atoms in cavity-generated dynamical optical potentials, Rev. Mod. Phys. **85**, 553 (2013).

[42] J. Klinder, H. Keßler, M. R. Bakhtiari, M. Thorwart, and A. Hemmerich, Observation of a superradiant Mott insulator in the Dicke-Hubbard model, Phys. Rev. Lett. **115**, 230403 (2015).

[43] J. Cohn, A. Safavi-Naini, R. J. Lewis-Swan, J. G. Bohnet, M. Gärttner, K. A. Gilmore, J. E. Jordan, A. M. Rey, J. J. Bollinger, and J. K. Freericks, Bang-bang shortcut to adiabaticity in the Dicke model as realized in a Penning trap experiment, New J. Phys. **20**, 055013 (2018).

[44] A. Safavi-Naini, R. J. Lewis-Swan, J. G. Bohnet, M. Gärttner, K. A. Gilmore, J. E. Jordan, J. Cohn, J. K. Freericks, A. M. Rey, and J. J. Bollinger, Verification of a many-ion simulator of the Dicke model through slow quenches across a phase transition, Phys. Rev. Lett. **121**, 040503 (2018).

[45] M. P. Baden, K. J. Arnold, A. L. Grimsmo, S. Parkins, and M. D. Barrett, Realization of the Dicke model using cavity-assisted Raman transitions, Phys. Rev. Lett. **113**, 020408 (2014).

[46] Z. Zhang, C. H. Lee, R. Kumar, K. J. Arnold, S. J. Masson, A. L. Grimsmo, A. S. Parkins, and M. D. Barrett, Dicke-model simulation via cavity-assisted Raman transitions, Phys. Rev. A **97**, 043858 (2018).

[47] P. Pérez-Fernández, A. Relaño, J. M. Arias, P. Cejnar, J. Dukelsky, and J. E. García-Ramos, Excited-state phase transition and onset of chaos in quantum optical models, Phys. Rev. E **83**, 046208 (2011).

[48] J. Chávez-Carlos, M. A. Bastarrachea-Magnani, S. Lerma-Hernández, and J. G. Hirsch, Classical chaos in atom-field systems, Phys. Rev. E **94**, 022209 (2016).

[49] W. Buijsman, V. Gritsev, and R. Sprik, Nonergodicity in the anisotropic Dicke model, Phys. Rev. Lett. **118**, 080601 (2017).

[50] F. Mattiotti, J. Dubail, D. Hagenmüller, J. Schachenmayer, J.-P. Brantut, and G. Pupillo, Multifractality in the interacting disordered Tavis-Cummings model, Phys. Rev. B **109**, 064202 (2024).

[51] P. Das and A. Sharma, Revisiting the phase transitions of the Dicke model, Phys. Rev. A **105**, 033716 (2022).

[52] P. Das, D. S. Bhakuni, and A. Sharma, Phase transitions of the anisotropic Dicke model, Phys. Rev. A **107**, 043706 (2023).

[53] G. Paladin and A. Vulpiani, Anomalous scaling laws in multifractal objects, Phys. Rep. **156**, 147 (1987).

[54] C. Godreche and J. M. Luck, Multifractal analysis in reciprocal space and the nature of the fourier transform of self-similar structures, J. Phys. A: Math. Gen. **23**, 3769 (1990).

[55] E. Ott, *Chaos in Dynamical Systems*, 2nd ed. (Cambridge University Press, Cambridge, UK, 2002).

[56] H. Hentschel and I. Procaccia, The infinite number of generalized dimensions of fractals and strange attractors, Physica D **8**, 435 (1983).

[57] T. C. Halsey, M. H. Jensen, L. P. Kadanoff, I. Procaccia, and B. I. Shraiman, Fractal measures and their singularities: The characterization of strange sets, Phys. Rev. A **33**, 1141 (1986).

[58] J. Balatoni and A. Renyi, Remarks on entropy, Publ. Math. Inst. Hung. Acad. Sci **1**, 9 (1956).

[59] P. Grassberger and I. Procaccia, Measuring the strangeness of strange attractors, Physica D **9**, 189 (1983).

[60] M. Janssen, Multifractal analysis of broadly-distributed observables at criticality, Int. J. Mod. Phys. B **08**, 943 (1994).

[61] F. Evers and A. D. Mirlin, Anderson transitions, Rev. Mod. Phys. **80**, 1355 (2008).

[62] R. J. Bell and P. Dean, Atomic vibrations in vitreous silica, Discuss. Faraday Soc. **50**, 55 (1970).

[63] D. Thouless, Electrons in disordered systems and the theory of localization, Phys. Rep. **13**, 93 (1974).

[64] C. Monthus, B. Berche, and C. Chatelain, Symmetry relations for multifractal spectra at random critical points, J. Stat. Mech.: Theory Exp. (2009) P12002.

[65] E. Bogomolny and O. Giraud, Multifractal dimensions for all moments for certain critical random-matrix ensembles in the strong multifractality regime, Phys. Rev. E **85**, 046208 (2012).

[66] A. Mildenberger and F. Evers, Wave function statistics at the symplectic two-dimensional Anderson transition: Bulk properties, Phys. Rev. B **75**, 041303(R) (2007).

[67] A. Rodriguez, L. J. Vasquez, and R. A. Römer, Optimisation of multifractal analysis at the 3D Anderson transition using box-size scaling, Eur. Phys. J. B **67**, 77 (2009).

[68] H. Obuse, A. R. Subramaniam, A. Furusaki, I. A. Gruzberg, and A. W. W. Ludwig, Conformal invariance, multifractality, and finite-size scaling at Anderson localization transitions in two dimensions, Phys. Rev. B **82**, 035309 (2010).

[69] A. Mildenberger, A. R. Subramaniam, R. Narayanan, F. Evers, I. A. Gruzberg, and A. D. Mirlin, Boundary multifractality in critical one-dimensional systems with long-range hopping, Phys. Rev. B **75**, 094204 (2007).

[70] F. Evers, A. Mildenberger, and A. D. Mirlin, Multifractality at the quantum Hall transition: Beyond the parabolic paradigm, Phys. Rev. Lett. **101**, 116803 (2008).

[71] A. M. Bilen, B. Georgeot, O. Giraud, G. Lemarié, and I. García-Mata, Symmetry violation of quantum multifractality: Gaussian fluctuations versus algebraic localization, Phys. Rev. Res. **3**, L022023 (2021).

[72] M. A. M. de Aguiar, K. Furuya, C. H. Lewenkopf, and M. C. Nemes, Particle-spin coupling in a chaotic system: Localization-delocalization in the Husimi distributions, Europhys. Lett. **15**, 125 (1991).

[73] M. de Aguiar, K. Furuya, C. Lewenkopf, and M. Nemes, Chaos in a spin-boson system: Classical analysis, Ann. Phys. **216**, 291 (1992).

[74] M. A. Bastarrachea-Magnani, S. Lerma-Hernández, and J. G. Hirsch, Comparative quantum and semiclassical analysis of atom-field systems. I. Density of states and excited-state quantum phase transitions, Phys. Rev. A **89**, 032101 (2014).

[75] M. A. Bastarrachea-Magnani, S. Lerma-Hernández, and J. G. Hirsch, Comparative quantum and semiclassical analysis of atom-field systems. II. Chaos and regularity, Phys. Rev. A **89**, 032102 (2014).

[76] M. A. Bastarrachea-Magnani, B. López-del-Carpio, S. Lerma-Hernández, and J. G. Hirsch, Chaos in the Dicke model: Quantum and semiclassical analysis, Phys. Scr. **90**, 068015 (2015).

[77] D. Villaseñor, S. Pilatowsky-Cameo, M. A. Bastarrachea-Magnani, S. Lerma, L. F. Santos, and J. G. Hirsch, Quantum vs classical dynamics in a spin-boson system: Manifestations of spectral correlations and scarring, New J. Phys. **22**, 063036 (2020).

[78] W.-M. Zhang, D. H. Feng, and R. Gilmore, Coherent states: Theory and some applications, Rev. Mod. Phys. **62**, 867 (1990).

[79] K. Hepp and E. H. Lieb, On the superradiant phase transition for molecules in a quantized radiation field: The Dicke-Maser model, Ann. Phys. (NY) **76**, 360 (1973).

[80] K. Hepp and E. H. Lieb, Equilibrium statistical mechanics of matter interacting with the quantized radiation field, Phys. Rev. A **8**, 2517 (1973).

[81] Y. K. Wang and F. T. Hioe, Phase transition in the Dicke model of superradiance, Phys. Rev. A **7**, 831 (1973).

[82] C. Emary and T. Brandes, Chaos and the quantum phase transition in the Dicke model, Phys. Rev. E **67**, 066203 (2003).

[83] M. A. Bastarrachea-Magnani and J. G. Hirsch, Efficient basis for the Dicke model: I. Theory and convergence in energy, Phys. Scr. **2014**, 014005 (2014).

[84] J. G. Hirsch and M. A. Bastarrachea-Magnani, Efficient basis for the Dicke model: II. Wave function convergence and excited states, Phys. Scr. **2014**, 014018 (2014).

[85] S. Pilatowsky-Cameo, D. Villaseñor, M. A. Bastarrachea-Magnani, S. Lerma-Hernández, and J. G. Hirsch, Effective dimensions of infinite-dimensional hilbert spaces: A phase-space approach, Phys. Rev. E **105**, 064209 (2022).

[86] S. Lerma-Hernández, J. Chávez-Carlos, M. A. Bastarrachea-Magnani, L. F. Santos, and J. G. Hirsch, Analytical description of the survival probability of coherent states in regular regimes, J. Phys. A **51**, 475302 (2018).

[87] D. A. Zarate-Herrada, L. F. Santos, and E. J. Torres-Herrera, Generalized survival probability, Entropy **25**, 205 (2023).

[88] A. Relaño, M. A. Bastarrachea-Magnani, and S. Lerma-Hernández, Approximated integrability of the Dicke model, Europhys. Lett. **116**, 50005 (2016).

[89] M. A. Bastarrachea-Magnani, B. López-del-Carpio, J. Chávez-Carlos, S. Lerma-Hernández, and J. G. Hirsch, Regularity and chaos in cavity QED, Phys. Scr. **92**, 054003 (2017).

[90] G. M. Zaslavskiî, R. Z. Sagdeev, D. A. Usikov, and A. A. Chernikov, *Weak Chaos and Quasi-Regular Patterns*, edited by A. R. Sagdeeva, Cambridge Nonlinear Science Series (Cambridge University Press, Cambridge, UK, 1991).

[91] L. E. Reichl and W. M. Zheng, Nonlinear resonance and chaos in conservative systems, in *Directions in Chaos–Volume 1* (World Scientific Publishing, Singapore, 1987), pp. 17–90.

[92] K. Hashimoto, K. Murata, and R. Yoshii, Out-of-time-order correlators in quantum mechanics, J. High Energy Phys. 10 (2017) 138.

[93] P. Cejnar, P. Stránský, M. Macek, and M. Kloc, Excited-state quantum phase transitions, J. Phys. A Math. **54**, 133001 (2021).

[94] Y. Y. Atas and E. Bogomolny, Multifractality of eigenfunctions in spin chains, Phys. Rev. E **86**, 021104 (2012).

[95] S. Lerma-Hernández, D. Villaseñor, M. A. Bastarrachea-Magnani, E. J. Torres-Herrera, L. F. Santos, and J. G. Hirsch, Dynamical signatures of quantum chaos and relaxation time scales in a spin-boson system, Phys. Rev. E **100**, 012218 (2019).

[96] J. Chávez-Carlos, B. López-del-Carpio, M. A. Bastarrachea-Magnani, P. Stránský, S. Lerma-Hernández, L. F. Santos, and J. G. Hirsch, Quantum and classical Lyapunov exponents in atom-field interaction systems, Phys. Rev. Lett. **122**, 024101 (2019).

[97] D. Tiwari and S. Banerjee, Quantum chaos in the Dicke model and its variants, Proc. R. Soc. A **479**, 20230431 (2023).

[98] G. Lemarié, H. Lignier, D. Delande, P. Szriftgiser, and J. C. Garreau, Critical state of the Anderson transition: Between a metal and an insulator, Phys. Rev. Lett. **105**, 090601 (2010).

[99] Y. Sagi, M. Brook, I. Almog, and N. Davidson, Observation of anomalous diffusion and fractional self-similarity in one dimension, Phys. Rev. Lett. **108**, 093002 (2012).

[100] M. Lopez, J.-F. Clément, G. Lemarié, D. Delande, P. Szriftgiser, and J. C. Garreau, Phase diagram of the anisotropic Anderson transition with the atomic kicked rotor: Theory and experiment, New J. Phys. **15**, 065013 (2013).

[101] A. Richardella, P. Roushan, S. Mack, B. Zhou, D. A. Huse, D. D. Awschalom, and A. Yazdani, Visualizing critical correlations near the metal-insulator transition in $Ga_{1-x}Mn_xAs$, Science **327**, 665 (2010).

[102] S. Faez, A. Strybulevych, J. H. Page, A. Lagendijk, and B. A. van Tiggelen, Observation of multifractality in Anderson localization of ultrasound, Phys. Rev. Lett. **103**, 155703 (2009).

[103] R. J. Lewis-Swan, A. Safavi-Naini, J. J. Bollinger, and A. M. Rey, Unifying scrambling, thermalization and entanglement through measurement of fidelity out-of-time-order correlators in the Dicke model, Nat. Commun. **10**, 1581 (2019).

[104] J. G. Bohnet, B. C. Sawyer, J. W. Britton, M. L. Wall, A. M. Rey, M. Foss-Feig, and J. J. Bollinger, Quantum spin dynamics and entanglement generation with hundreds of trapped ions, Science **352**, 1297 (2016).

[105] R. J. Lewis-Swan, S. R. Muleady, D. Barberena, J. J. Bollinger, and A. M. Rey, Characterizing the dynamical phase diagram of the Dicke model via classical and quantum probes, Phys. Rev. Res. **3**, L022020 (2021).

[106] I. García-Mata, O. Giraud, and B. Georgeot, Quantum computation of multifractal exponents through the quantum wavelet transform, Phys. Rev. A **79**, 052321 (2009).

[107] J. Schliemann, Coherent quantum dynamics: What fluctuations can tell, Phys. Rev. A **92**, 022108 (2015).